catalysts

MDPI

Article

Synthesis of Magnetic $Fe_3O_4/ZnWO_4$ and $Fe_3O_4/ZnWO_4/CeVO_4$ Nanoparticles: The Photocatalytic Effects on Organic Pollutants upon Irradiation with UV-Vis Light

Mohammad Amin Marsooli [1,2], Mehdi Rahimi Nasrabadi [1,2,*], Mahdi Fasihi-Ramandi [1], Kourosh Adib [3], Saeid Pourmasoud [4], Farhad Ahmadi [5,6], Mohammad Eghbali [4], Ali Sobhani Nasab [7,8,*], Monika Tomczykowa [9] and Marta E. Plonska-Brzezinska [9,*]

[1] Molecular Biology Research Center, Systems Biology and Poisoning Institute, Baqiyatallah University of Medical Sciences, Sheikh Bahaei Street, Tehran 1951683759, Iran; mohammadamin.marsuli@gmail.com (M.A.M.); fasihi.m@gmail.com (M.F.-R.)
[2] Faculty of Pharmacy, Baqiyatallah University of Medical Sciences, Sheikh Bahaei Street, Tehran 1951683759, Iran
[3] Department of Chemistry, Imam Hossein University, Babaei Highway, Tehran 1955735345, Iran; k_anbaz@yahoo.com
[4] Department of Physics, University of Kashan, Ravand Street, Kashan 8731753153, Iran; SA_PO2007@yahoo.com (S.P.); SA_POURMASOUD2007@yahoo.com (M.E.)
[5] Physiology Research Center, Iran University of Medical Sciences, Hemmat Highway, Tehran 1449614535, Iran; Farhadahmadi55@gmail.com
[6] Department of Medicinal Chemistry, School of Pharmacy-International Campus, Iran University of Medical Sciences, Hemmat Highway, Tehran 1451555763, Iran
[7] Social Determinants of Health (SDH) Research Center, Kashan University of Medical Sciences, Kashan 8115187159, Iran
[8] Core Research Lab, Kashan University of Medical Sciences, Ravand Street, Kashan 8115187159, Iran
[9] Department of Organic Chemistry, Faculty of Pharmacy with the Division of Laboratory Medicine, Medical University of Bialystok, Mickiewicza 2A, 15-222 Bialystok, Poland; monika.tomczyk@umb.edu.pl
* Correspondence: rahiminasrabadi@gmail.com (M.R.N.); ali.sobhaninasab@gmail.com (A.S.N.); marta.plonska-brzezinska@umb.edu.pl (M.E.P.-B.); Tel.: +98-2182-483409 (M.R.N.)

Received: 12 March 2020; Accepted: 22 April 2020; Published: 1 May 2020

Abstract: Magnetic $Fe_3O_4/ZnWO_4$ and $Fe_3O_4/ZnWO_4/CeVO_4$ nanoparticles with different molar ratios of $CeVO_4$ to other inorganic components were synthesized through co-precipitation with a sonochemical-assisted method. X-ray diffraction, energy dispersive X-ray spectroscopy, Fourier transform infrared spectroscopy, ultraviolet-visible diffuse reflectance spectroscopy, vibrating sample magnetometry, and scanning electron microscopy (SEM) methods were used for the physico–chemical characterization of the obtained nanoparticles. As shown in the SEM images, the average sizes of the $Fe_3O_4/ZnWO_4$ and $Fe_3O_4/ZnWO_4/CeVO_4$ nanoparticles that formed aggregates were approximately 50–70 nm and 80–100 nm, respectively. The photocatalytic performance of these nanoparticles was examined by measuring methylene blue degradation under visible light (assisted by H_2O_2). The sample with a mass ratio of 1:2:1 ($Fe_3O_4/ZnWO_4/CeVO_4$, S_4) exhibited optimal photocatalytic performance, and thus this sample was subsequently used for the photodegradation of different organic pollutants upon irradiation with ultraviolet (UV) and visible light. Approximately 90% and 70% degradation of methyl violet and methylene blue, respectively, was observed after visible light irradiation. Additionally, the mechanism of the photocatalytic reaction was investigated by measuring $^{\cdot}OH$ release under UV light in a system with terephthalic acid and by measuring the release of $^{\cdot}O_2^{-}$, $^{\cdot}OH$, and hole scavengers.

Keywords: magnetic nanoparticles; Fe_3O_4; $CdWO_4$; $CeVO_4$; sonochemical procedure; photocatalysis

---

1. Introduction

The development of human civilization across the earth in the form of population growth and increasing industrialization has resulted in a shortage of healthy wastewater. Wastewater may contain many pathogenic microorganisms and pharmaceutical and chemical residues [1–4]. A large variety of organic compounds are capable of being completely degraded and mineralized into CO_2 and harmless inorganic anions. The chemical and pharmaceutical pollutants may include, but are not limited to salts, metalloids, metals, organic compounds, residual drugs, endocrine-disrupting compounds [5–7], and other compounds. Therefore, different methods have been proposed to treat water resources and restore good and healthy properties to water. Different chemical and biological methods have been used to purify industrial, agricultural, and pharmaceutical wastewater and increase the number of existing resources available [8–10].

Photocatalytic processes have become an attractive method for researchers to use to degrade pollutants [11–15]. "Photocatalysis" is a catalytic process driven by light in nature and uses materials called "photocatalysts". Photocatalysis was first reported at the beginning of the nineteenth century, but a boom took place in the field of heterogeneous photocatalysis after an article reported photo-assisted catalysis of water upon irradiation of TiO_2 [16]. Semiconductors are frequently used for this process, due to their optical properties, electronic structure, and intrinsic nature [17–21]. Many physical and chemical parameters affect the efficiency of photocatalytic processes, including (i) their chemical composition, such as the elemental composition and chemical state/structure; (ii) physical properties, such as the physical and crystal structures, optical absorption, charge dynamics, defects, and thermal stability; and (iii) band structure (band gap, band edges and Fermi level) [22]. An appropriate band gap is one of the main principles of a photocatalyst [23]. A suitable band gap is important because of the ability to capture light and its effect on redox reactions that are performed by photocatalytic systems designed by incorporating a matrix into the semiconductor or by adding a co-catalyst [24–27].

Photocatalysis, in which a photoinduced chemical reaction occurs on the surface of semiconductor materials (photocatalyst) upon exposure to photons, is a heterogeneous process [14,28]. Photocatalysts are typically composed of metal oxides, oxysulfides, metal sulfides, oxynitrides, their composites [23,29–35], and other materials. The chemical structure and the well-developed surface (morphology) of the materials exert significant effects on the photocatalytic process. The ability to tune the functional and morphological properties of nanocrystals is one of the most important issue in photocatalysis [15], mainly because the size, shape, and porous characteristics of synthesized nanomaterials affect the photocatalytic properties of these materials [34,36–39].

Magnetizing photocatalytic materials is a procedure to easily split a photocatalyst after use. One of the challenges facing the use of photocatalysts is the leakage of metal ions from the catalyst. The use of magnetic nanoparticles reduces the likelihood of metal leakage because the particles might have accumulated an external magnetic field. The most effective magnetic particles are those containing iron oxide core because of their low cost, easy separation, and excellent reusability [40–45]. Fe_3O_4 has unique electronic and magnetic characteristics that are the result of complicated electron–electron and electron–phonon interactions [42]. The introduction of other metals into these materials containing iron oxides creates multiferroic systems, which can be developed by exploiting the epitaxial strain, oxygen vacancy, charge, or composition gradients [42]. To conclude, multiferroic heterostructures may have enhanced heterogeneous catalytic activity and selectivity compared with monometallic materials [40,41,44] Among the substantial number of multiferroic heterostructures, one of the main groups is metal tungstates, with the formula of MWO_4 (M = Co, Cu, Zn, Pb, and Mn), and transition metal-based orthovanadates (MVO_4) [42,46–48]. Metal tungstates possess interesting structural and photoluminescence properties, mainly including ferroelasticity, ionic conductivity, and photoluminescence [47,49]. Due to their very interesting physico–chemical and nanostructural properties, they have attracted the interest of researchers in many areas. In particular, $ZnWO_4$ has been used in various applications, such as sensors, scintillators, laser hosts, and phase-change optical recording devices [50,51]. In some situations, $ZnWO_4$ is used to photodegrade organic pollutants [37]. Additionally, MVO_4 materials are a cohesive class of materials with potential applications in various fields, such as optoelectronics, spintronics, catalysis, solar cells, gas sensors, photoluminescence, and photocatalysis [35,52–54]. Although these two groups of inorganic oxides possess very good photocatalytic properties and degrade organic pollutants, a major problem after their use is their removal from wastewater after the redox reaction. The solution to this problem is to use a photocatalyst with magnetic properties. By preparing nanoparticles or composites with simultaneous photocatalytic and magnetic properties, the used photocatalysts can be extracted for recycling with an external magnetic field [55].

Here, the facile synthesis of magnetic $Fe_3O_4/ZnWO_4/CeVO_4$ nanoparticles at different molar ratios of $CeVO_4$ to $Fe_3O_4/ZnWO_4$ is reported. The molar ratios of subsequent layers were as follows: 1:2:0.5 (designated as S_2), 1:2:0.75 (designated as S_3), 1:2:1 (designated as S_4), and 1:2:1.5 (designated as S_5). The photocatalytic activities of these samples upon irradiation with visible light were compared with $Fe_3O_4/ZnWO_4$ (designated as S_1) as a reference. The structural, morphological, optical, and magnetic properties of the photocatalysts were determined for the nanoparticles with the highest photocatalytic activity—S_4 (1:2:1). Three dye pollutants, methylene blue (MB), methyl orange (MO), and methyl violet (MV), were employed to measure the photocatalytic activity of the samples after irradiation with visible light (assisted by H_2O_2, MB was used in an optimization step as a probe). The efficiency of the synthesized samples illuminated with ultraviolet light was tested using MB, fenitrothion (FNT), MO, and rhodamine-B (RhB). The conversion of terephthalic acid (TA) to 2-hydroxy-terephthalic acid in the presence of hydroxyl radicals and with the assistance of $^{\cdot}O_2{}^{-}$, $^{\cdot}OH$ and hole scavengers was analysed to investigate the mechanism of the photocatalytic reaction.

2. Results

2.1. Physico–Chemical Characterization of $Fe_3O_4/ZnWO_4$ and $Fe_3O_4/ZnWO_4/CeVO_4$ Nanoparticles

X-ray diffraction (XRD) was performed to identify the phase composition and to determine the metal crystallite size and size distribution of the synthesized inorganic nanoparticles (Fe_3O_4, $Fe_3O_4/ZnWO_4$, and $Fe_3O_4/ZnWO_4/CeVO_4$ (S_4)). The results of the XRD analyses are shown in Figure 1. Figure 1a shows the diffraction pattern for Fe_3O_4, with the main diffraction peaks observed at 2θ of 35.6° (line (311)) and of 63.1° (line (220)), which correspond to the cubic phases of Fe_3O_4 (72-2303 JCPDS) [56]. The average crystallite size (D_c) was calculated using the well-known Scherrer formula:

$$D_C = \frac{K\lambda}{\beta \cos\theta} \tag{1}$$

where λ is the X-ray wavelength (nm), β is the breadth of the observed diffraction line at half its intensity maximum [57,58], and K is a constant (0.9) related to the crystallite shape for any 2θ peak in the pattern [59,60]. The average D_c value was calculated and was ca. 15 nm. $Fe_3O_4/ZnWO_4$ (Figure 1b) was composed of two pure phases of Fe_3O_4 (JCPDS 72-2303) and $ZnWO_4$ (JCPDS 15-0774), with diffraction peaks at the positions of 35.6°, 63.1°, 30.47°, 53.63°, and 64.78° that corresponded to the lines (311), (220), (111), (202), and (311), respectively. The D_c value was estimated as 36.3 nm. The S_4 profile revealed the presence of a mixture of various phases (Figure 1c).

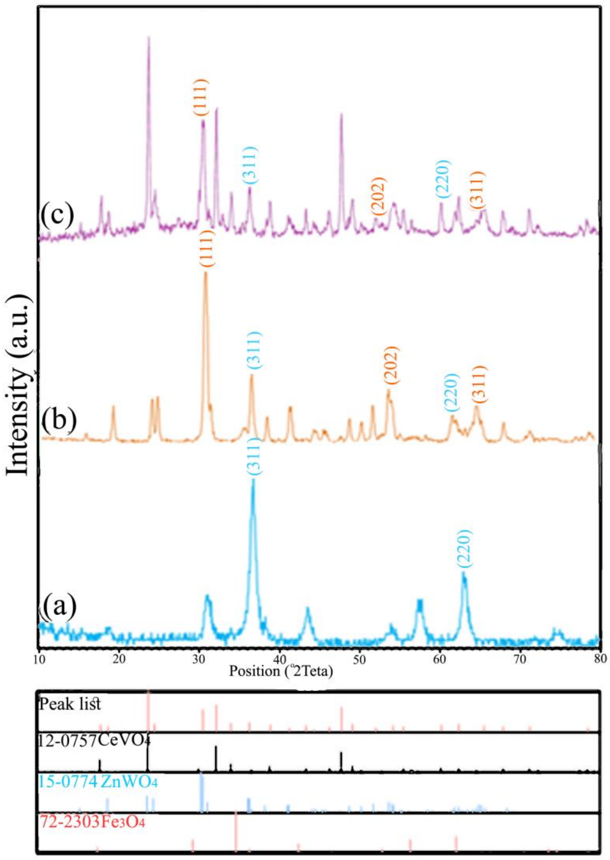

Figure 1. XRD patterns of (**a**) Fe_3O_4, (**b**) $Fe_3O_4/ZnWO_4$ (S_1), and (**c**) $Fe_3O_4/ZnWO_4/CeVO_4$ (S_4).

The $Fe_3O_4/ZnWO_4/CeVO_4$ nanoparticles presented a combination of three pure phases of Fe_3O_4 (JCPDS 72-2303) [61], $ZnWO_4$ (JCPDS 15-0774) [62], and $CeVO_4$ (JCPDS 12-0757) [63]. The diffraction peaks were observed at 2θ of 24.03° (line (200)), 32.04° (line (112)), and 47.86° (line (312)), consistent with a pure phase tetragonal $CeVO_4$ nanostructure [64]. The D_c value for the nanohybrid system increased to 58 nm (Figure 1c). All calculated parameters are summarized in Table 1. In summary, the profiles of all inorganic nanoparticles confirmed the presence of Fe_3O_4, $ZnWO_4$, and $CeVO_4$ components in the obtained materials.

Table 1. Main reflections observed in the XRD patterns of inorganic nanoparticles.

Sample	2 Theta (Degrees)	hkl	Crystallite Sizes Dhkl (nm)	Average Crystallite Size (nm)	A (Å)	B (Å)	C (Å)
Fe_3O_4	35.6 63.1	(311) (220)	15.8 14.3	0.15	8.3740	8.3740	8.3740
$Fe_3O_4/ZnWO_4$	35.6 63.1 30.47 53.63 64.78	(311) (220) (111) (202) (311)	16.33 15.40 12.60 13.62 14.79	36.3	4.6910	5.7200	4.9250
$Fe_3O_4/ZnWO_4/CeVO_4$	35.6 63.1 30.47 53.63 64.78 24.03 32.40 47.86	(311) (220) (111) (202) (311) (200) (112) (322)	16.68 16.01 14.02 15.32 16.14 14.63 12.67 11.96	58.7	7.3990	7.3990	6.4960

An energy dispersive X-ray (EDX) analysis of the $Fe_3O_4/ZnWO_4/CeVO_4$ (S_4) material was performed to confirm the purity of the synthesized nanoparticles and the presence of individual elements (Figure 2f). Figure 2f displays the presence of subsequent elements, W, Fe, Zn, O, Ce, and V, in $Fe_3O_4/ZnWO_4/CeVO_4$. The atomic ratio of these elements in this nanoparticle were as follows: 12.81 (Fe), 54.35 (O), 5.63 (Zn), 7.81 (W), 6.19 (Ce), and 13.21% (V).

The morphology of the obtained materials was examined using scanning electron microscopy (SEM), and the results are presented in Figure 2. The SEM images indicate the difference between the nanoparticles with different molar ratios of inorganic components (Fe_3O_4 and $ZnWO_4$ and $CeVO_4$) and they do not exhibit single and separated $Fe_3O_4/ZnWO_4/CeVO_4$ nanoparticles. The inorganic nanoparticles were formed by nanoclusters, with a different distribution following a concentration-dependent process (Figure 2b–e). The smallest $Fe_3O_4/ZnWO_4/CeVO_4$ aggregates formed the sample with the molar ratios of 1:2:1 (S_4). The agglomerates of $Fe_3O_4/ZnWO_4/CeVO_4$ nanoparticles with different dimensions formed a spongy-like structure with an increasing diameter after the deposition of subsequent inorganic layers. An average size of 50–70 nm for S_1 and 80–100 nm for S_4 was determined based on these results (Figure 2a,d, respectively). Additionally, the results confirmed that the size of the nanoparticle aggregates obtained from the SEM images was larger than the size identified using XRD. The SEM images show the diameters of various crystallites created after the evaporation of the solvent in which the nanoparticles were dispersed.

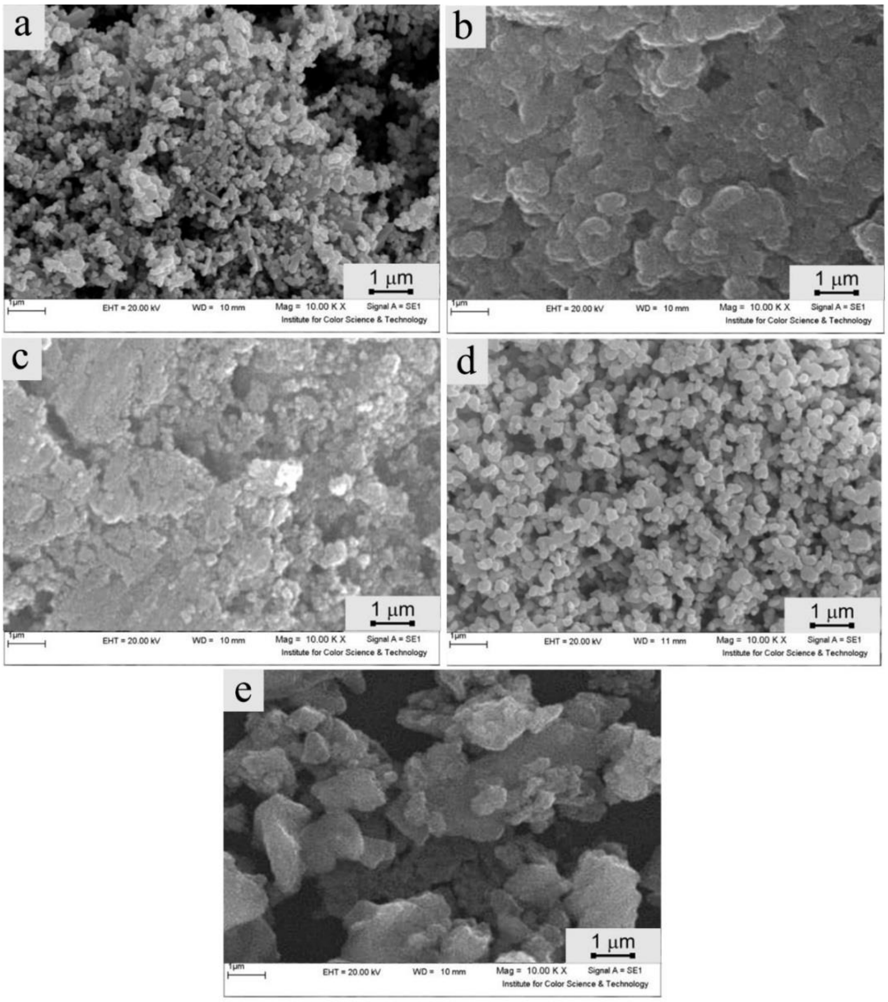

Figure 2. *Cont.*

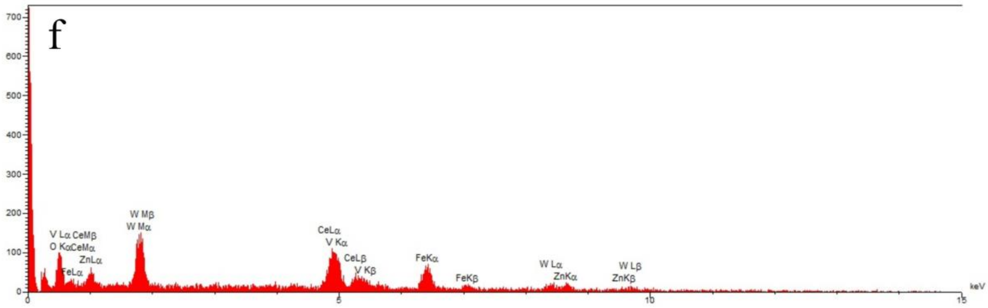

Figure 2. SEM images of (**a**) $Fe_3O_4/ZnWO_4$ (S_1), and $Fe_3O_4/ZnWO_4/CeVO_4$ with the molar ratios of (**b**) 1:2:0.5 (S_2), (**c**) 1:2:0.75 (S_3), (**d**) 1:2:1 (S_4), and (**e**) 1:2:1.5 (S_5). (**f**) EDX spectrum of the $Fe_3O_4/ZnWO_4/CeVO_4$ (S_4) sample.

Figure 3 shows the magnetic hysteresis loops of (a) Fe_3O_4 and (b) $Fe_3O_4/ZnWO_4/CeVO_4$ (S_4) at 300 K. As shown in this figure, Fe_3O_4 and $Fe_3O_4/ZnWO_4/CeVO_4$ displayed magnetization saturation (M_s) values of 50.9 and 1.5 emu g^{-1}, respectively. The saturation magnetization of $Fe_3O_4/ZnWO_4/CeVO_4$ nanoparticles was lower than that of unmodified Fe_3O_4, which is related to the additional inorganic layers ($ZnWO_4/CeVO_4$). However, the magnetization of $Fe_3O_4/ZnWO_4/CeVO_4$ nanoparticles was sufficient for the magnetic separation of photocatalysts from the treated solution using an external magnetic field.

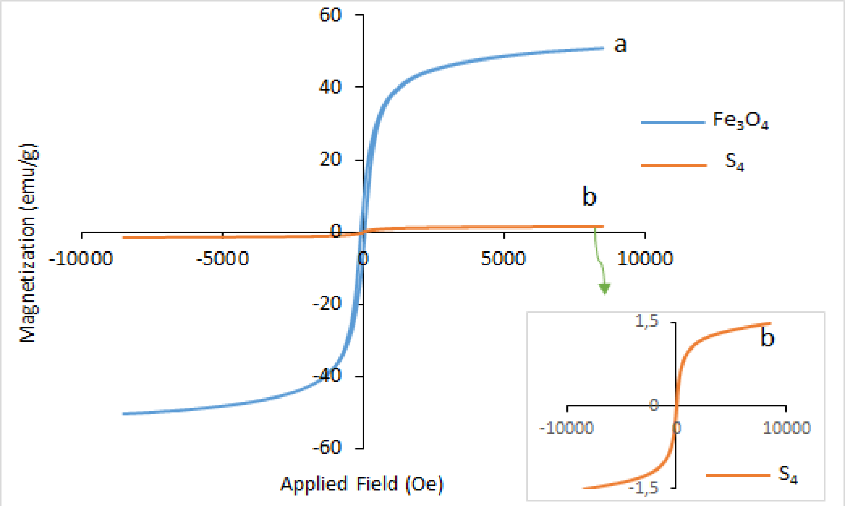

Figure 3. Magnetic hysteresis loops of (**a**) Fe_3O_4 and (**b**) $Fe_3O_4/ZnWO_4/CeVO_4$.

The light absorption properties of materials play a significant role in their photocatalytic activities [63]. The relationship between the energy and absorption edge was calculated using Tauc's Equation [65]:

$$\alpha h\upsilon = A\left(h\upsilon - E_g\right)^{\eta} \tag{2}$$

where h is Planck's constant, υ is the frequency of light, α is the absorption coefficient, E_g is the optical band gap energy (OBGE), A is a constant, and η is 0.5 or 2 for direct or indirect transitions, respectively. The value of $\eta = 2$ was considered in this experiment [66]. Based on the data shown in Tauc's plot of the S_1 and S_4 samples (Figure 4), the OBGE values were ca. 3.1 and 2.6 eV, respectively. Generally, the OBGE values may be affected by the surface and interface effect, change in crystal structure, and lattice strain in the structure [67]. However, the S_1 sample had a higher OBGE value; a combination of Fe_3O_4 conductivity with visible light active semiconductivity is frequently required for photocatalytic purposes. Herein, we report $Fe_3O_4/ZnWO_4/CeVO_4$ hierarchical core-shell structures that enhanced the electron-hole separation (Fe_3O_4) and light harvesting ($ZnWO_4$/$CeVO_4$) due to their multifunctionality and synergetic effect on every component [68].

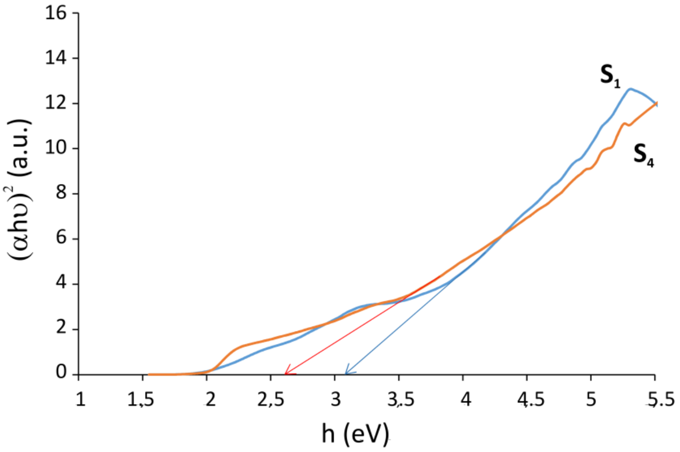

Figure 4. Tauc's plot of the S_1 and S_4 samples.

Fourier transform infrared spectroscopy (FTIR) was performed to assess the chemical structure of Fe_3O_4, Fe_3O_4/$ZnWO_4$ (S_1), Fe_3O_4/$ZnWO_4$/$CeVO_4$ (S_4) (before and after calcination), and S_4 after the photocatalytic removal of MB at a concentration of 25 mg L^{-1}. The measurements were conducted in the range of 500–3500 cm^{-1}, and the outcomes are presented in Figure 5. The bands at 3390–3410 and 1620–1638 cm^{-1} were assigned to the O–H stretching vibration due to the presence of surface hydroxyl groups and H_2O. In Figure 5a, the absorption peak observed at 587 cm^{-1} is attributed to the Fe–O vibration from the magnetite phase [69]. The absorption band at 620 cm^{-1} originated from symmetrical vibrations of the bridging oxygen atoms of the Zn–O–W groups (Figure 5b) [70]. The absorption bands at 820 and 888 cm^{-1} are attributed to the vibration of the WO_2 units in the W_2O_8 system. Figure 5c,d show the FTIR spectra of the S_4 sample before and after calcination, respectively. The peaks at 839 and 822 cm^{-1} represent the V-O vibration frequency [64,71].

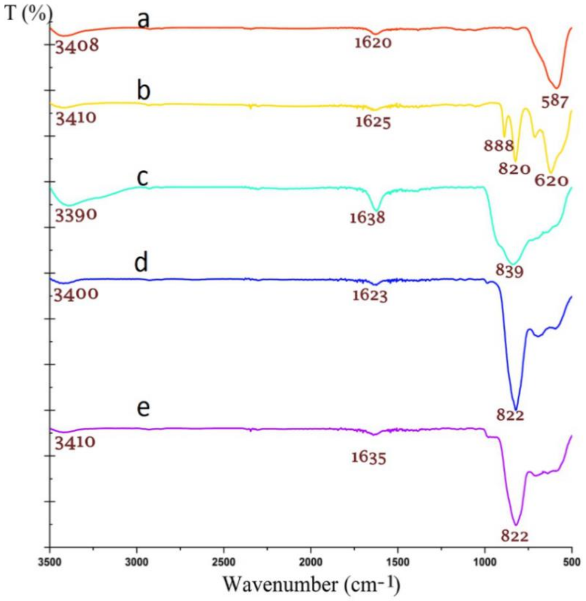

Figure 5. FTIR spectra of (**a**) Fe_3O_4, (**b**) the S_1 sample, (**c**) the S_4 sample before calcination, (**d**) the S_4 sample after calcination, and (**e**) S_4 after the photodegradation of MB.

Figure 5e shows the FTIR spectrum of S_4 after the photodegradation of MB (25 ppm) upon irradiation with UV light. The lack of change in the peak indicates that the photocatalyst was not altered during the photocatalytic reaction. Based on the FTIR data, light irradiation in the presence of organic pollutants did not affect or destroy the chemical structure of the obtained inorganic nanoparticles. Therefore, the FTIR studies confirmed the incorporation of the three inorganic phases into one system and their high environmental stability under light irradiation, indicating that these nanostructures were successfully used as photocatalytic materials to remove pollutants.

2.2. *Photocatalytic Reactions Using $Fe_3O_4/ZnWO_4/CeVO_4$*

Figure 6a shows the photocatalytic degradation of 25 mg L^{-1} MB by the synthesized samples (along with 1 mL of H_2O_2 in 100 mL of MB) to determine an optimal catalyst and compare the performance of H_2O_2 in the presence and absence of the catalysts. Additionally, Figure 6b shows a plot of the kinetics of $-\ln(C/C_0)$ versus the irradiation time. Figure 6c shows temporal changes in the absorption spectra of MB during the photodegradation mediated by the S_4 sample. The slope of the linear regression curve was calculated as the first-order reaction rate constant. As shown in Figure 6a, S_4 exhibited the best performance among all synthesized samples and was capable of removing the organic pollutant via photocatalysis.

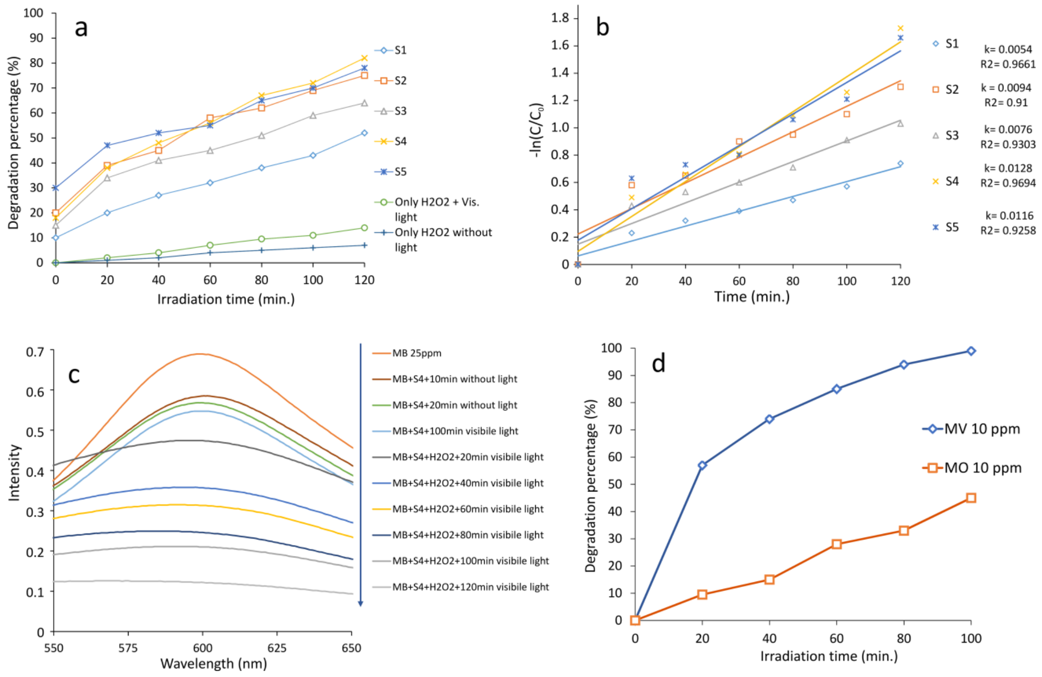

Figure 6. (**a**) Photocatalytic degradation of MB (1–5 samples) under visible light assisted by H_2O_2. (**b**) Pseudo-first-order kinetics of MB degradation by samples 1–5. (**c**) Temporal changes in the absorption spectra of MB during the photodegradation mediated by the S_4 sample. (**d**) Photocatalytic degradation of the MV and MO pollutants by the S_4 sample under visible light assisted by H_2O_2.

Similar experiments for S_4 were conducted to measure the photodegradation of MV and MO, and the results are shown in Figure 6d. The photodegradation of MV was much higher than that of MO. After of exposure to light irradiation for 100 min, 90% of MV was degraded. Similarly, under the same experimental conditions, less MO was degraded, approximately 50% of the initial concentration, by the S_4 sample.

A photocatalytic degradation test was performed using different contaminants, MB, MO, fenitrothion (FNT, O,O-dimethyl-O-4-nitro-*m*-tolyl phosphorothioate), and rhodamine-B (RhB), to examine the photocatalytic efficiency of S_4 upon irradiation with UV light. The results are shown in Figure 7. After approximately 70 min of exposure to light, the lowest photocatalytic activity of S_4 was observed for FNT. This is an organophosphorus pesticide that exhibits high chemical stability and resistance to biodegradation [72,73]. Pesticides degrade very slowly under light irradiation compared with the reaction rates obtained using photocatalysts [74].

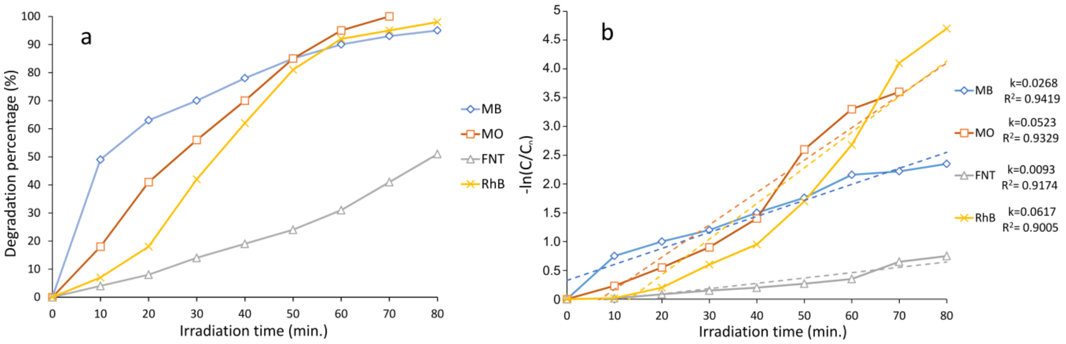

Figure 7. (**a**) Photocatalytic degradation of MB, MO, FNT, and RhB by the S_4 sample under UV light irradiation. (**b**) Pseudo-first-order kinetics of MB, MO, FNT, and RhB degradation by the S_4 sample.

The addition of some inorganic and organic matter is necessary to increase the photodegradation efficiency of photocatalysts because these substances may affect the photodegradation rate due to their adsorption on the catalyst surface [75]. On the other hand, efficient photodegradation of MB, MO, and RhB by S_4 was observed.

The mechanisms of photocatalytic reactions were examined by capturing hydroxyl radicals ($^{\cdot}$OH). Hydroxyl radicals are usually sensed with the terephthalic acid (TA) photoluminescence probing method [76–78]. Following the adsorption of $^{\cdot}$OH by TA, 2-hydroxyl-terephthalic acid is produced and displays fluorescence emission; therefore, $^{\cdot}$OH is able to be sensed by monitoring the changes in the fluorescence intensity of the TA solution. Figure 8 shows the variations in the fluorescence intensity of 2-hydroxyl-terephthalic acid at 443 nm. As shown in Figure 8, with increasing UV irradiation time, the fluorescence intensity increased. However, in the first 10 min without irradiation, the intensity of the $^{\cdot}$OH signal was minimized, indicating that $^{\cdot}$OH was produced over the photocatalyst during UV irradiation.

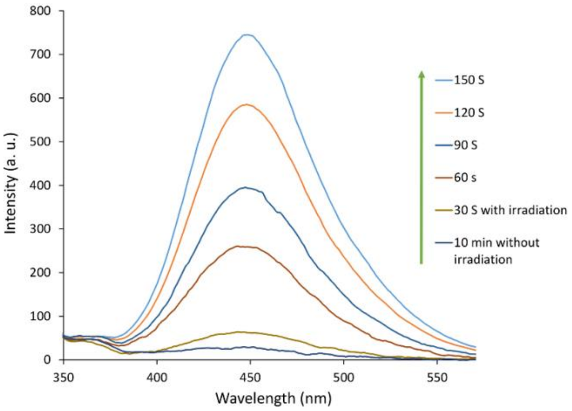

Figure 8. The temporal changes in the fluorescence intensity of 2-hydroxyl-terephthalic acid upon irradiation with UV light (290 nm) in the presence of S_4.

The principal oxidative species in the photocatalytic process was identified by performing trapping tests of $^{\cdot}$OH, superoxide radical ($^{\cdot}O_2^-$), and holes using tert-butanol, benzoquinone, and citric acid, respectively [64,71]. The results of the experiments conducted using these scavengers to measure the photodegradation of MB (25 ppm) are shown in Figure 9a. After the addition of the superoxide scavenger, the photocatalyst performance was substantially reduced (by approximately 75%). Furthermore, the addition of the hydroxyl scavenger decreased the photocatalytic performance by approximately 50%. In contrast, the addition of the hole scavenger exerted a slight effect on photocatalytic performance. Based on these results, the $^{\cdot}OH$ and $^{\cdot}O_2{}^-$ radicals were the main oxidative species photogenerated by the synthesized nanoparticles. Figure 9b presents the proposed graphical mechanism of the photocatalytic reaction in the presence of H_2O_2. This mechanism was determined and described in detail in our previous study [65].

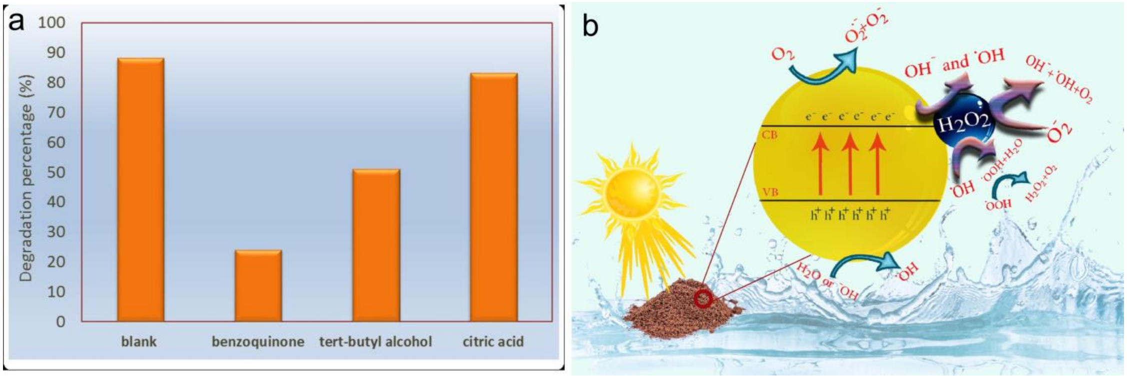

Figure 9. (**a**) Effects of different scavengers (benzoquinone, tert-butyl alcohol, and citric acid) on the photocatalytic degradation of MB. (**b**) Proposed graphical mechanism of the photocatalytic reaction.

The photocatalytic activity of semiconductors is very complicated and can be affected by factors such as the chemical structure, composition, material size, surface area, and a suitable band gap. Briefly, considering a magnetic nanoparticle as a photocatalyst, the magnetic core is useful for the separation of the photocatalyst from treated water whereas the outer inorganic layer is beneficial for the photocatalytic reaction [44]. Some examples of Fe_3O_4-based photocatalysts are presented in Table 2.

Table 2. Some examples of Fe_3O_4-based photocatalysts and their photocatalytic parameters.

Samples	Light Source	Pollutant	Degradation (%)	The Amount of Catalyst Used (g/100 mL)	Time (min)	Ref.
Fe_3O_4/TiO_2 (120 nm)	UV	RhB	5.4	0.1	50	[79]
Fe_3O_4/TiO_2 (420 nm)	UV	RhB	25.8	0.1	50	[79]
$Fe_3O_4/ZnWO_4$	UV	RhB	100	0.1	300	[80]
Fe_3O_4/Ag_2WO_4	Vis.	Fast green	81	-	120	[81]
$Fe_3O_4/CdWO_4$	Vis.	MB	32	0.02	120	[62]
$Fe_3O_4/CdWO_4/PrVO_4$	Vis.	MB	68	0.02	120	[62]
Bi_2WO_6	Vis.	RhB	62.5	-	180	[82]
Fe_3O_4/Bi_2WO_6	Vis.	RhB	95.8	-	180	[82]
Fe_3O_4/Bi_2WO_6	Vis.	RhB	66	0.1	180	[83]
$Fe_3O_4/SiO_2/Bi_2WO_6$	Vis.	RhB	100	-	100	[82]
ZnO	UV	MB	80	0.01	60	[84]
Fe_3O_4/ZnO	UV	MB	94	0.01	60	[84]
$Fe_3O_4/Zn_xCd_{1\text{-}c}S$	Vis.	MB	92	0.01	35	[85]
$Fe_3O_4/ZnWO_4/CeVO_4$	Vis	MB	84	0.02	120	**This work**

Application of pristine Fe_3O_4 in photocatalysis is limited owing to its easy aggregation and its easy electron–hole recombination [44]. To eliminate these shortcomings, the modification of Fe_3O_4 is required by designing core-shell nanostructures (Table 2). The Fe_3O_4-based nanocomposites have higher chemical and photochemical stability, higher photocatalytic activity, and are reusable and magnetically recoverable. For example, introducing inert substances, such as ceramics (SiO_2), can protect Fe_3O_4 from chemical dissolution and can affect photocatalytic processes [79]. By controlling the thickness of the outer inorganic shell, increased degradation of pollutants might be achieved [80].

The smaller photocatalytic nanoparticles are more active than larger ones. With decreasing size of the semiconductor crystal size, the recombination rate of e^-/h^+ pairs will decrease [67]. Additionally, smaller nanoparticles with larger specific areas have a higher photon absorption rate on the surface of photons. These findings were observed for our $Fe_3O_4/ZnWO_4/CeVO_4$ nanoparticles with the different molar ratios of the three components (Figure 2). Briefly, comparison of the pristine inorganic nanoparticles with the nanocomposites clearly showed that the improved photocatalytic activity of the multilayered nanoparticles was ascribed to efficient electron–hole separation.

In summary, we suggest that the synergetic effect of triple-layer inorganic nanoparticles (Fe_3O_4 and $ZnWO_4$ and $CeVO_4$) leads to enhancement of photocatalytic activity under visible light irradiation (Table 2). In this regard, the $Fe_3O_4/ZnWO_4/CeVO_4$ nanoparticles (with molar ratios of 1:2:1) are found to be effective as a simple recyclable photocatalytic material for removing organic pollutants from wastewater.

3. Materials and Methods

3.1. Materials

Unless noted, all chemicals and solvents were commercially available and used as received without further purification from Sigma, Germany. We used iron (III) chloride hexahydrate ($FeCl_3{\cdot}6H_2O$) (99%), iron (II) chloride tetrahydrate ($FeCl_2{\cdot}4H_2O$) (99%), sodium hydroxide (NaOH) (98%), zinc chloride ($ZnCl_2$) (98%), zinc tungstate ($ZnWO_4$) (99%), sodium tungstate dehydrate ($Na_2WO_4{\cdot}2H_2O$) (99%), cerium (III) nitrate hexahydrate ($Ce(NO_3)_3{\cdot}6H_2O$) (99%), ammonium metavanadate (NH_4VO_3) (99%), methyl orange (MO) (99%), methylene blue (MB) (99%), methyl violet (MV) (99%), fenitrothion (FNT) (99%), rhodamine B (RhB) (99%) and ethanol (99.8%). All aqueous solutions were made using deionized water, which was further purified with a Milli-Q system (Millipore).

3.2. Synthesis of Fe_3O_4 Nanoparticles

The co-precipitation method was used to synthesize the Fe_3O_4 nanoparticles. First, 16.25 g of $FeCl_3$ and 6.32 g of $FeCl_2$ were dissolved in 200 mL of distilled water and stirred with a mechanical stirrer for 60 min. Then, precipitation was induced by adding 2 M NaOH at 30 °C in an N_2 atmosphere. The reaction system was maintained at a temperature of 70 °C for 5 h, while maintaining the pH of the solution at ± 12. Next, the system was cooled to room temperature, and the precipitate was separated with a permanent magnet and washed with distilled water to obtain a neutral pH. Finally, Fe_3O_4 nanoparticles were washed with acetone and dried at 70 °C [58].

3.3. Synthesis of $Fe_3O_4/ZnWO_4$ Nanoparticles

The $Fe_3O_4/ZnWO_4$ nanoparticles were synthesized using the in situ co-precipitation method. First, 0.232 g of the previously obtained Fe_3O_4 nanoparticles were dispersed in 50 mL of distilled water using ultrasonication for 20 min. Then, 0.274 g of $ZnCl_2$ dissolved in 50 mL of distilled water was added to the reactor containing Fe_3O_4. The reaction mixture was stirred for 10 min at room temperature using a mechanical stirrer. Then, a solution prepared by dissolving 0.66 g of $Na_2WO_4{\cdot}2H_2O$ in 50 mL of distilled water was added to this mixture dropwise over 10 min, and the whole solution was mixed using ultrasonication. The resulting precipitate was filtered/separated with a magnet, washed twice with distilled water and once with ethanol, and dried in an oven at 70 °C. Finally, the synthesized $Fe_3O_4/ZnWO_4$ nanoparticles were placed in an oven for calcination (3 h at 550 °C).

3.4. Synthesis of $Fe_3O_4/ZnWO_4/CeVO_4$ Nanoparticles

For this reaction, 0.544 g of $Fe_3O_4/ZnWO_4$ prepared in the previous step was dispersed in 50 mL of distilled water and ultrasonicated for 20 min. Then, 0.058 g of NH_4VO_3 and 0.217 g of $Ce(NO_3)_3{\cdot}6H_2O$, were separately dissolved in 50 mL of distilled water to prepare a precipitate with a molar ratio of 1:2:0.5. The NH_4VO_3 solution was added to the previously dispersed nanoparticles. The mixture was subjected to ultrasonication with a probe with a power of 400 W and frequency of 20 KHz. Afterwards, the $Ce(NO_3)_3{\cdot}6H_2O$ solution was added dropwise to the mixture, and the reaction continued for the next 15 min. Quantities of 0.087 g of NH_4VO_3 and 0.325 g of $Ce(NO_3)_3{\cdot}6H_2O$, 0.117 g of NH_4VO_3, and 0.44 g of $Ce(NO_3)_3{\cdot}6H_2O$, as well as 0.175 g of NH_4VO_3 and 0.651 g of $Ce(NO_3)_3{\cdot}6H_2O$, were used to prepare precipitates with molar ratios of 1:2:0.75, 1:2:1, and 1:2:1.5, respectively. The obtained precipitates were washed twice with distilled water and once with ethanol and then dried in an oven at 70 °C. Finally, the synthesized $Fe_3O_4/ZnWO_4/CeVO_4$ nanoparticles were placed in an oven for calcination (3 h at 550 °C).

3.5. Evaluation of Photocatalytic Activities

The photodegradation of MB under visible light was measured for all synthesized samples to choose the nanoparticles with the highest photocatalytic activity. In each experiment, 60 mg of photocatalyst was added to 300 mL of a 25 mg L^{-1} MB solution. Three milliliters of 25% H_2O_2 were added to the photoreactor to increase the efficacy. Prior to exposure to visible light (250 W xenon lamp), the solution was stirred in the dark for 20 min to obtain an adsorption/desorption equilibrium between the catalyst and MB. Four milliliters of the solution were collected with a pipette every 10 min for the reaction conducted in the dark and every 20 min for the reaction conducted in the light. Then, the studied solution was centrifuged at 5000 rpm for 5 min to separate the catalyst. The concentration of the MB solution was calculated by recording the absorption with a UV–Vis spectrophotometer to identify the result of the photodegradation of pollutants. Afterwards, the sample with the optimized photocatalytic properties (the highest value of degradation) was used for the photodegradation of 10 mg L^{-1} MO and 10 mg L^{-1} MV.

The photocatalytic activity of S_4 was evaluated by analyzing the photodegradation of MB under UV light to determine the efficiency of the synthesized photocatalyst. In each experiment, 30 mg of photocatalyst was added to 300 mL of the 20 mg/L MB solution. Prior to exposure to the UV light, (50 W Hg lamp), the solution was stirred in the dark for 20 min to obtain an adsorption/desorption equilibrium between the catalyst and MB solution. Next, 4 mL of the solution were pipetted every 10 min and centrifuged at 5000 rpm for 5 min to separate the catalyst. As described above, the concentration of the MB solution was calculated by measuring the absorbance with a UV–Vis spectrophotometer to estimate the yield of photodegradation. Afterwards, the material with the optimal photocatalytic properties was used to photodegrade 15 mg L^{-1} MO, 15 mg L^{-1} FNT, and 20 mg L^{-1} RhB.

3.6. Photodegradation Mechanism

The release of $^{\cdot}OH$ was measured using a photoluminescence method. 2-Hydroxyterephthalic acid is the product of the reaction of TA with $^{\cdot}OH$, which has fluorescence properties. Hence, the fluorescence intensity depends on the amount of $^{\cdot}OH$ released. The method is similar to photocatalytic tests conducted under UV light. The solution was prepared by adding 0.03 g of the synthesized catalyst (0.1 g L^{-1}) to 300 mL of the aqueous TA solutions prepared at concentrations of 0.0005 M and 0.002 M in NaOH. The principal oxidative factor in the photocatalytic reactions was identified by measuring the amounts of $^{\cdot}O_2^{-}$, $^{\cdot}OH$, and holes trapped by tert-butanol, benzoquinone, and citric acid, respectively. The procedure is similar to the UV irradiation test. Three hundred milliliters of a 25 mg L^{-1} MB solution were prepared, and then 3 mmol of one of the scavengers were added to that solution. Afterwards, 0.03 g of dispersed photocatalyst was added to the system. Finally, after exposing the solution to UV light, 4 mL of the solution was removed from the reactor every 10 min and the catalyst was separated from the pollutant by centrifugation. The progress of each reaction was monitored using a UV–Vis spectrophotometer.

4. Conclusions

The $Fe_3O_4/ZnWO_4/CeVO_4$ nanoparticles were prepared at different molar ratios using the co-precipitation method with the help of the sonochemical method. Identification tests, such as

XRD, SEM, FTIR, and EDX, confirmed the presence of the subsequent inorganic phases: Fe_3O_4, $ZnWO_4$, and $CeVO_4$. The VSM test allowed us to calculate the MS values for Fe_3O_4 and the $Fe_3O_4/ZnWO_4/CeVO_4$ nanoparticles: 50.9 and 1.5 emu g^{-1}, respectively. Additionally, based on the results of the DRS test, the OBGEs for Fe_3O_4 and $Fe_3O_4/ZnWO_4/CeVO_4$ were 3.1 and 2.6 eV, respectively. The $Fe_3O_4/ZnWO_4/CeVO_4$ nanoparticles with a 1:2:1 molar ratio mediated the highly efficient photocatalytic degradation of different organic pollutants, such as MV with ~100% degradation (with visible light) and MO with ~100% degradation (under UV light). When $Fe_3O_4/ZnWO_4/CeVO_4$ (S_4) was reacted in the presence of various scavengers, the photogenerated $^{\cdot}OH$ and $^{\cdot}O_2^{-}$ radicals were the main oxidative forms, and the fluorescence intensities increased over time upon the irradiation of TA with UV–Vis light, which produced $^{\cdot}OH$ as a by-product. These results confirm that the $Fe_3O_4/ZnWO_4/CeVO_4$ nanoparticles represent a potentially useful photocatalyst for the effective removal of organic pollutants from wastewater.

Author Contributions: Conceptualization, M.A.M., M.R.N., and A.S.N.; statistical analysis, M.A.M., M.R.N., and A.S.N.; writing—original draft preparation, M.A.M, M.R.N., A.S.N., M.F.-R., K.A., S.P., F.A. and M.E.; methodology and writing—review and editing, M.E.P.-B. and M.T.; and funding acquisition, M.R.N., M.E.P.-B., and M.T. All authors approved the final version for submission. All authors have read and agreed to the published version of the manuscript.

Funding: We gratefully acknowledge the financial support from Iran University of Medical Sciences to M.R.N. and from the Ministry of Science and Higher Education, Poland (SUB/2/DN/20/001/2204) to M.E.P.-B. This study was supported by Council of Baqiyatallah University of Medical Sciences through grant agreement No. 95221.

Conflicts of Interest: The authors have no conflicts of interest to declare.

References

1. Franz, S.; Falletta, E.; Arab, H.; Murgolo, S.; Bestetti, M.; Mascolo, G. Degradation of Carbamazepine by Photo(electro)catalysis on Nanostructured TiO_2 Meshes: Transformation Products and Reaction Pathways. *Catalysts* **2020**, *10*, 169. [CrossRef]
2. Li, S.; Xue, B.; Chen, J.; Jiang, W.; Liu, Y. BiOCOOH Microflowers Decorated with Ag/Ag_2CrO_4 Nanoparticles as Highly Efficient Photocatalyst for the Treatment of Toxic Wastewater. *Catalysts* **2020**, *10*, 93. [CrossRef]
3. Feijoo, S.; González-Rodríguez, J.; Fernández, L.; Vázquez-Vázquez, C.; Feijoo, G.; Moreira, M.T. Fenton and Photo-Fenton Nanocatalysts Revisited from the Perspective of Life Cycle Assessment. *Catalysts* **2019**, *10*, 23. [CrossRef]
4. Włodarczyk, P.P.; Włodarczyk, B. Preparation and Analysis of Ni–Co Catalyst Use for Electricity Production and COD Reduction in Microbial Fuel Cells. *Catalysts* **2019**, *9*, 1042. [CrossRef]
5. Khalid, S.; Shahid, M.; Natasha Bibi, I.; Sarwar, T.; Shah, A.; Niazi, N. A Review of Environmental Contamination and Health Risk Assessment of Wastewater Use for Crop Irrigation with a Focus on Low and High-Income Countries. *Int. J. Environ. Res. Public Health* **2018**, *15*, 895. [CrossRef]
6. Schaider, L.A.; Rodgers, K.M.; Rudel, R.A. Review of Organic Wastewater Compound Concentrations and Removal in Onsite Wastewater Treatment Systems. *Environ. Sci. Technol.* **2017**, *51*, 7304–7317. [CrossRef]
7. Bartolomeu, M.; Neves, M.G.P.M.S.; Faustino, M.A.F.; Almeida, A. Wastewater chemical contaminants: Remediation by advanced oxidation processes. *Photochem. Photobiol. Sci.* **2018**, *17*, 1573–1598. [CrossRef]
8. Holkar, C.R.; Jadhav, A.J.; Pinjari, D.V.; Mahamuni, N.M.; Pandit, A.B. A critical review on textile wastewater treatments: Possible approaches. *J. Environ. Manag.* **2016**, *182*, 351–366. [CrossRef]
9. Kweinor Tetteh, E.; Rathilal, S.; Chetty, M.; Kwaku Armah, E.; Asante-Sackey, D. Treatment of Water and Wastewater for Reuse and Energy Generation-Emerging Technologies. In *Water and Wastewater Treatment*; Eyvaz, M., Ed.; IntechOpen: London, UK, 2019; ISBN 978-1-78923-929-4.
10. Singh, N.B.; Nagpal, G.; Agrawal, S. Rachna Water purification by using Adsorbents: A Review. *Environ. Technol. Innov.* **2018**, *11*, 187–240. [CrossRef]
11. Eghbali-Arani, M.; Sobhani-Nasab, A.; Rahimi-Nasrabadi, M.; Pourmasoud, S. Green Synthesis and Characterization of $SmVO_4$ Nanoparticles in the Presence of Carbohydrates as Capping Agents with Investigation of Visible-Light Photocatalytic Properties. *J. Electron. Mater.* **2018**, *47*, 3757–3769. [CrossRef]

12. Zinatloo-Ajabshir, S.; Mortazavi-Derazkola, S.; Salavati-Niasari, M. Preparation, characterization and photocatalytic degradation of methyl violet pollutant of holmium oxide nanostructures prepared through a facile precipitation method. *J. Mol. Liq.* **2017**, *231*, 306–313. [CrossRef]
13. Shon, J.-H.; Teets, T.S. Photocatalysis with Transition Metal Based Photosensitizers. *Comments Inorg. Chem.* **2020**, *40*, 53–85. [CrossRef]
14. Xu, C.; Ravi Anusuyadevi, P.; Aymonier, C.; Luque, R.; Marre, S. Nanostructured materials for photocatalysis. *Chem. Soc. Rev.* **2019**, *48*, 3868–3902. [CrossRef]
15. Luciani, G.; Imparato, C.; Vitiello, G. Photosensitive Hybrid Nanostructured Materials: The Big Challenges for Sunlight Capture. *Catalysts* **2020**, *10*, 103. [CrossRef]
16. Fujishima, A.; Honda, K. Electrochemical Photolysis of Water at a Semiconductor Electrode. *Nature* **1972**, *238*, 37–38. [CrossRef] [PubMed]
17. Xiang, Q.; Yu, J.; Jaroniec, M. Graphene-based semiconductor photocatalysts. *Chem. Soc. Rev.* **2012**, *41*, 782–796. [CrossRef] [PubMed]
18. Wang, H.; Zhang, L.; Chen, Z.; Hu, J.; Li, S.; Wang, Z.; Liu, J.; Wang, X. Semiconductor heterojunction photocatalysts: Design, construction, and photocatalytic performances. *Chem. Soc. Rev.* **2014**, *43*, 5234. [CrossRef]
19. Chen, X.; Shen, S.; Guo, L.; Mao, S.S. Semiconductor-based Photocatalytic Hydrogen Generation. *Chem. Rev.* **2010**, *110*, 6503–6570. [CrossRef]
20. Hisatomi, T.; Kubota, J.; Domen, K. Recent advances in semiconductors for photocatalytic and photoelectrochemical water splitting. *Chem. Soc. Rev.* **2014**, *43*, 7520–7535. [CrossRef]
21. Chen, Y.; Bai, X. A Review on Quantum Dots Modified g-C_3N_4-Based Photocatalysts with Improved Photocatalytic Activity. *Catalysts* **2020**, *10*, 142. [CrossRef]
22. Zhang, L.; Ran, J.; Qiao, S.-Z.; Jaroniec, M. Characterization of semiconductor photocatalysts. *Chem. Soc. Rev.* **2019**, *48*, 5184–5206. [CrossRef] [PubMed]
23. Moreno-Castilla, C.; López-Ramón, M.V.; Fontecha-Cámara, M.Á.; Álvarez, M.A.; Mateus, L. Removal of Phenolic Compounds from Water Using Copper Ferrite Nanosphere Composites as Fenton Catalysts. *Nanomaterials* **2019**, *9*, 901. [CrossRef] [PubMed]
24. Lv, J.; Dai, K.; Zhang, J.; Lu, L.; Liang, C.; Geng, L.; Wang, Z.; Yuan, G.; Zhu, G. In situ controllable synthesis of novel surface plasmon resonance-enhanced Ag_2WO_4/Ag/Bi_2MoO_6 composite for enhanced and stable visible light photocatalyst. *Appl. Surf. Sci.* **2017**, *391*, 507–515. [CrossRef]
25. Sobhani-Nasab, A.; Pourmasoud, S.; Ahmadi, F.; Wysokowski, M.; Jesionowski, T.; Ehrlich, H.; Rahimi-Nasrabadi, M. Synthesis and characterization of $MnWO_4$/$TmVO_4$ ternary nano-hybrids by an ultrasonic method for enhanced photocatalytic activity in the degradation of organic dyes. *Mater. Lett.* **2019**, *238*, 159–162. [CrossRef]
26. Peymani-Motlagh, S.M.; Moeinian, N.; Rostami, M.; Fasihi-Ramandi, M.; Sobhani-Nasab, A.; Rahimi-Nasrabadi, M.; Eghbali-Arani, M.; Ganjali, M.R.; Jesionowski, T.; Ehrlich, H.; et al. Effect of Gd3+-, Pr3+- or Sm3+-substituted cobalt–zinc ferrite on photodegradation of methyl orange and cytotoxicity tests. *J. Rare Earths* **2019**, *37*, 1288–1295. [CrossRef]
27. Gandomi, F.; Peymani-Motlagh, S.M.; Rostami, M.; Sobhani-Nasab, A.; Fasihi-Ramandi, M.; Eghbali-Arani, M.; Ahmadian, R.; Gholipour, N.; Rahimi-Nasrabadi, M.; Ganjali, M.R. Simple synthesis and characterization of $Li_{0.5}Fe_{2.5}O_4$, $LiMg_{0.5}Fe_2O_4$ and $LiNi_{0.5}Fe_2O_4$, and investigation of their photocatalytic and anticancer properties on hela cells line. *J. Mater. Sci. Mater. Electron.* **2019**, *30*, 19691–19702. [CrossRef]
28. Chiu, Y.-H.; Chang, T.-F.M.; Chen, C.-Y.; Sone, M.; Hsu, Y.-J. Mechanistic Insights into Photodegradation of Organic Dyes Using Heterostructure Photocatalysts. *Catalysts* **2019**, *9*, 430. [CrossRef]
29. Wang, Q.; Nakabayashi, M.; Hisatomi, T.; Sun, S.; Akiyama, S.; Wang, Z.; Pan, Z.; Xiao, X.; Watanabe, T.; Yamada, T.; et al. Oxysulfide photocatalyst for visible-light-driven overall water splitting. *Nat. Mater.* **2019**, *18*, 827–832. [CrossRef]
30. Zhang, G.; Wang, X. Oxysulfide Semiconductors for Photocatalytic Overall Water Splitting with Visible Light. *Angew. Chem. Int. Ed.* **2019**, *58*, 15580–15582. [CrossRef]
31. Hao, H.; Lang, X. Metal Sulfide Photocatalysis: Visible-Light-Induced Organic Transformations. *ChemCatChem* **2019**, *11*, 1378–1393. [CrossRef]
32. Ahmed, M.; Xinxin, G. A review of metal oxynitrides for photocatalysis. *Inorg. Chem. Front.* **2016**, *3*, 578–590. [CrossRef]

33. Polo, A.M.S.; Lopez-Peñalver, J.J.; Sánchez-Polo, M.; Rivera-Utrilla, J.; López-Ramón, M.V.; Rozalén, M. Halide removal from water using silver doped magnetic-microparticles. *J. Environ. Manag.* **2020**, *253*, 109731. [CrossRef] [PubMed]
34. Wang, K.; Janczarek, M.; Wei, Z.; Raja-Mogan, T.; Endo-Kimura, M.; Khedr, T.M.; Ohtani, B.; Kowalska, E. Morphology- and Crystalline Composition-Governed Activity of Titania-Based Photocatalysts: Overview and Perspective. *Catalysts* **2019**, *9*, 1054. [CrossRef]
35. Melinte, V.; Stroea, L.; Chibac-Scutaru, A.L. Polymer Nanocomposites for Photocatalytic Applications. *Catalysts* **2019**, *9*, 986. [CrossRef]
36. Kar, A.; Sain, S.; Kundu, S.; Bhattacharyya, A.; Kumar Pradhan, S.; Patra, A. Influence of Size and Shape on the Photocatalytic Properties of SnO_2 Nanocrystals. *ChemPhysChem* **2015**, *16*, 1017–1025. [CrossRef] [PubMed]
37. Pereira, P.F.S.; Gouveia, A.F.; Assis, M.; de Oliveira, R.C.; Pinatti, I.M.; Penha, M.; Gonçalves, R.F.; Gracia, L.; Andrés, J.; Longo, E. $ZnWO_4$ nanocrystals: Synthesis, morphology, photoluminescence and photocatalytic properties. *Phys. Chem. Chem. Phys.* **2018**, *20*, 1923–1937. [CrossRef]
38. Zhang, W. Preparation, morphology, size quantization effect and photocatalytic properties of CdS Q-nanocrystals. *Sci. China Ser. B* **2003**, *46*, 196–206. [CrossRef]
39. Li, Y.-F.; Liu, Z.-P. Particle Size, Shape and Activity for Photocatalysis on Titania Anatase Nanoparticles in Aqueous Surroundings. *J. Am. Chem. Soc.* **2011**, *133*, 15743–15752. [CrossRef] [PubMed]
40. Jin, H.; Tian, X.; Nie, Y.; Zhou, Z.; Yang, C.; Li, Y.; Lu, L. Oxygen Vacancy Promoted Heterogeneous Fenton-like Degradation of Ofloxacin at pH 3.2–9.0 by Cu Substituted Magnetic Fe_3O_4@FeOOH Nanocomposite. *Environ. Sci. Technol.* **2017**, *51*, 12699–12706. [CrossRef]
41. Lu, Z.; Zhao, X.; Zhu, Z.; Yan, Y.; Shi, W.; Dong, H.; Ma, Z.; Gao, N.; Wang, Y.; Huang, H. Enhanced Recyclability, Stability, and Selectivity of CdS/C@Fe_3O_4 Nanoreactors for Orientation Photodegradation of Ciprofloxacin. *Chem. Eur. J.* **2015**, *21*, 18528–18533. [CrossRef]
42. Hou, X.; Wang, X.; Mi, W. Progress in Fe_3O_4-based multiferroic heterostructures. *J. Alloys Compd.* **2018**, *765*, 1127–1138. [CrossRef]
43. Mu, Q.; Sun, Y.; Guo, A.; Yu, X.; Xu, X.; Cai, A.; Wang, X. Bio-templated synthesis of Fe_3O_4–TiO_2 composites derived from Chlorella pyrenoidosa with enhanced visible-light photocatalytic performance. *Mater. Res. Express* **2019**, *6*, 0950c3. [CrossRef]
44. Mishra, P.; Patnaik, S.; Parida, K. An overview of recent progress on noble metal modified magnetic Fe_3O_4 for photocatalytic pollutant degradation and H_2 evolution. *Catal. Sci. Technol.* **2019**, *9*, 916–941. [CrossRef]
45. Amin Marsooli, M.; Rahimi Nasrabadi, M.; Fasihi-Ramandi, M.; Adib, K.; Eghbali, M.; Pourmasoud, S.; Ahmadi, F.; Sohouli, E.; Sobhani Nasab, A.; Ali Mirhosseini, S.; et al. Preparation of Fe_3O_4/SiO_2/TiO_2/$PrVO_4$ nanocomposite in various molar ratios: Investigation on photocatalytic performance on organic contaminate and bacterial environments, and anti-cancer properties. *Polyhedron* **2020**, *176*, 114239. [CrossRef]
46. Ke, J.; Adnan Younis, M.; Kong, Y.; Zhou, H.; Liu, J.; Lei, L.; Hou, Y. Nanostructured Ternary Metal Tungstate-Based Photocatalysts for Environmental Purification and Solar Water Splitting: A Review. *Nano-Micro Lett.* **2018**, *10*, 69. [CrossRef]
47. García-Pérez, U.M.; de la Cruz, A.M.; Peral, J. Transition metal tungstates synthesized by co-precipitation method: Basic photocatalytic properties. *Electrochim. Acta* **2012**, *81*, 227–232. [CrossRef]
48. Peng, W.; Li, Y.; Zhang, F.; Zhang, G.; Fan, X. Roles of Two-Dimensional Transition Metal Dichalcogenides as Cocatalysts in Photocatalytic Hydrogen Evolution and Environmental Remediation. *Ind. Eng. Chem. Res.* **2017**, *56*, 4611–4626. [CrossRef]
49. Zawawi, S.M.M.; Yahya, R.; Hassan, A.; Mahmud, H.E.; Daud, M.N. Structural and optical characterization of metal tungstates (MWO_4; M=Ni, Ba, Bi) synthesized by a sucrose-templated method. *Chem. Cent. J.* **2013**, *7*, 80. [CrossRef]
50. Kuzmin, A.; Kalendarev, R.; Kursitis, A.; Purans, J. Confocal spectromicroscopy of amorphous and nanocrystalline tungsten oxide films. *J. Non-Cryst. Solids* **2007**, *353*, 1840–1843. [CrossRef]
51. Hosseinpour-Mashkani, S.M.; Maddahfar, M.; Sobhani-Nasab, A. Precipitation Synthesis, Characterization, Morphological Control, and Photocatalyst Application of $ZnWO_4$ Nanoparticles. *J. Electron. Mater.* **2016**, *45*, 3612–3620. [CrossRef]

52. Hosseinpour-Mashkani, S.S.; Sobhani-Nasab, A. Investigation the effect of temperature and polymeric capping agents on the size and photocatalytic properties of NdVO4 nanoparticles. *J. Mater. Sci. Mater. Electron.* **2017**, *28*, 16459–16466. [CrossRef]
53. Tedstone, A.A.; Lewis, D.J.; O'Brien, P. Synthesis, Properties, and Applications of Transition Metal-Doped Layered Transition Metal Dichalcogenides. *Chem. Mater.* **2016**, *28*, 1965–1974. [CrossRef]
54. Lv, R.; Robinson, J.A.; Schaak, R.E.; Sun, D.; Sun, Y.; Mallouk, T.E.; Terrones, M. Transition Metal Dichalcogenides and Beyond: Synthesis, Properties, and Applications of Single- and Few-Layer Nanosheets. *Acc. Chem. Res.* **2015**, *48*, 56–64. [CrossRef] [PubMed]
55. Gómez-Pastora, J.; Dominguez, S.; Bringas, E.; Rivero, M.J.; Ortiz, I.; Dionysiou, D.D. Review and perspectives on the use of magnetic nanophotocatalysts (MNPCs) in water treatment. *Chem. Eng. J.* **2017**, *310*, 407–427. [CrossRef]
56. Lopez Maldonado, K.L.; de la Presa, P.; de la Rubia, M.A.; Crespo, P.; de Frutos, J.; Hernando, A.; Matutes Aquino, J.A.; Elizalde Galindo, J.T. Effects of grain boundary width and crystallite size on conductivity and magnetic properties of magnetite nanoparticles. *J. Nanoparticle Res.* **2014**, *16*, 2482. [CrossRef]
57. Smilgies, D.-M. Scherrer grain-size analysis adapted to grazing-incidence scattering with area detectors. *J. Appl. Crystallogr.* **2009**, *42*, 1030–1034. [CrossRef] [PubMed]
58. Zinatloo-Ajabshir, S.; Salavati-Niasari, M. Preparation and characterization of nanocrystalline praseodymium oxide via a simple precipitation approach. *J. Mater. Sci. Mater. Electron.* **2015**, *26*, 5812–5821. [CrossRef]
59. Monshi, A.; Foroughi, M.R.; Monshi, M.R. Modified Scherrer Equation to Estimate More Accurately Nano-Crystallite Size Using XRD. *World J. Nano Sci. Eng.* **2012**, *2*, 154–160. [CrossRef]
60. Umbrello, D.; Rotella, G.; Matsumura, T.; Musha, Y. Evaluation of microstructural changes by X-ray diffraction peak profile and focused ion beam/scanning ion microscope analysis. *Int. J. Adv. Manuf. Technol.* **2015**, *77*, 1465–1474. [CrossRef]
61. Zou, Z.; Xuan, A.G.; Yan, Z.G.; Wu, Y.X.; Li, N. Preparation of Fe_3O_4 particles from copper/iron ore cinder and their microwave absorption properties. *Chem. Eng. Sci.* **2010**, *65*, 160–164. [CrossRef]
62. Marsooli, M.A.; Fasihi-Ramandi, M.; Adib, K.; Pourmasoud, S.; Ahmadi, F.; Ganjali, M.R.; Sobhani Nasab, A.; Rahimi Nasrabadi, M.; Plonska-Brzezinska, M.E. Preparation and Characterization of Magnetic $Fe_3O_4/CdWO_4$ and $Fe_3O_4/CdWO_4/PrVO_4$ Nanoparticles and Investigation of Their Photocatalytic and Anticancer Properties on PANC1 Cells. *Materials* **2019**, *12*, 3274. [CrossRef] [PubMed]
63. Kalai Selvan, R.; Gedanken, A.; Anilkumar, P.; Manikandan, G.; Karunakaran, C. Synthesis and Characterization of Rare Earth Orthovanadate (RVO_4; R = La, Ce, Nd, Sm, Eu & Gd) Nanorods/Nanocrystals/Nanospindles by a Facile Sonochemical Method and Their Catalytic Properties. *J. Clust. Sci.* **2009**, *20*, 291–305.
64. Ekthammathat, N.; Thongtem, T.; Phuruangrat, A.; Thongtem, S. Synthesis and Characterization of $CeVO_4$ by Microwave Radiation Method and Its Photocatalytic Activity. *J. Nanomater.* **2013**, *2013*, 1–7.
65. Adib, K.; Rezvani, Z.; Rahimi-Nasrabadi, M.; Pourmortazavi, S.M. Statistically optimized synthesis of cadmium tungstate nanoplates for use as a photocatalyst. *J. Mater. Sci. Mater. Electron.* **2018**, *29*, 6377–6387. [CrossRef]
66. Beshkar, F.; Zinatloo-Ajabshir, S.; Salavati-Niasari, M. Preparation and characterization of the $CuCr_2O_4$ nanostructures via a new simple route. *J. Mater. Sci. Mater. Electron.* **2015**, *26*, 5043–5051. [CrossRef]
67. Deotale, A.J.; Nandedkar, R.V. Correlation between Particle Size, Strain and Band Gap of Iron Oxide Nanoparticles. *Mater. Today Proc.* **2016**, *3*, 2069–2076. [CrossRef]
68. Xi, G.; Yue, B.; Cao, J.; Ye, J. Fe3O4/WO3 Hierarchical Core-Shell Structure: High-Performance and Recyclable Visible-Light Photocatalysis. *Chem. Eur. J.* **2011**, *17*, 5145–5154. [CrossRef]
69. Yang, S.; Zeng, T.; Li, Y.; Liu, J.; Chen, Q.; Zhou, J.; Ye, Y.; Tang, B. Preparation of Graphene Oxide Decorated $Fe_3O_4@SiO_2$ Nanocomposites with Superior Adsorption Capacity and SERS Detection for Organic Dyes. *J. Nanomater.* **2015**, *2015*, 1–8.
70. Rahimi-Nasrabadi, M.; Pourmortazavi, S.M.; Ganjali, M.R.; Hajimirsadeghi, S.S.; Zahedi, M.M. Electrosynthesis and characterization of zinc tungstate nanoparticles. *J. Mol. Struct.* **2013**, *1047*, 31–36. [CrossRef]
71. Sadiq Mohamed, M.J.; Bhat Denthaje, K. Novel RGO-$ZnWO_4$-Fe_3O_4 Nanocomposite as an Efficient Catalyst for Rapid Reduction of 4-Nitrophenol to 4-Aminophenol. *Ind. Eng. Chem. Res.* **2016**, *55*, 7267–7272. [CrossRef]

72. Rawtani, D.; Khatri, N.; Tyagi, S.; Pandey, G. Nanotechnology-based recent approaches for sensing and remediation of pesticides. *J. Environ. Manag.* **2018**, *206*, 749–762. [CrossRef] [PubMed]
73. Topalov, A.; Molnár-Gábor, D.; Abramović, B.; Korom, S.; Peričin, D. Photocatalytic removal of the insecticide fenitrothion from water sensitized with TiO_2. *J. Photochem. Photobiol. Chem.* **2003**, *160*, 195–201. [CrossRef]
74. Vela, N.; Calín, M.; Yáñez-Gascón, M.J.; Garrido, I.; Pérez-Lucas, G.; Fenoll, J.; Navarro, S. Photocatalytic oxidation of six pesticides listed as endocrine disruptor chemicals from wastewater using two different TiO_2 samples at pilot plant scale under sunlight irradiation. *J. Photochem. Photobiol. Chem.* **2018**, *353*, 271–278. [CrossRef]
75. Ahmed, S.; Rasul, M.G.; Brown, R.; Hashib, M.A. Influence of parameters on the heterogeneous photocatalytic degradation of pesticides and phenolic contaminants in wastewater: A short review. *J. Environ. Manag.* **2011**, *92*, 311–330. [CrossRef]
76. Shifu, C.; Lei, J.; Wenming, T.; Xianliang, F. Fabrication, characterization and mechanism of a novel Z-scheme photocatalyst $NaNbO_3/WO_3$ with enhanced photocatalytic activity. *Dalton Trans.* **2013**, *42*, 10759. [CrossRef]
77. Ishibashi, K.; Fujishima, A.; Watanabe, T.; Hashimoto, K. Detection of active oxidative species in TiO2 photocatalysis using the fluorescence technique. *Electrochem. Commun.* **2000**, *2*, 207–210. [CrossRef]
78. Ibrahim, A.M.A.; Al-Ashqar, S.M.A. Spectroscopic and kinetic studies on the degradation of methylene blue using the supramolecular coordination polymer [(Ph_3Sn)4Fe(CN)6] as catalyst. *Spectrochim. Acta. A Mol. Biomol. Spectrosc.* **2012**, *92*, 238–244. [CrossRef]
79. Choi, K.-H.; Oh, S.-L.; Kim, D.-Y.; Jung, J.-S. Size Dependent Photocatalytic Activity of Photofunctional Magnetic Core–Shell (Fe_3O_4@ TiO_2) Particles. *J. Nanosci. Nanotechnol.* **2013**, *13*, 7134–7137. [CrossRef]
80. Zhou, Y.X.; Tong, L.; Chen, X.B.; Zeng, X.H. Fe3O4-ZnWO4 hybrid microspheres: Facile synthesis and magnetically recyclable photocatalytic performance. *Micro-Nano Lett.* **2013**, *8*, 32–34. [CrossRef]
81. Rajamohan, S.; Kumaravel, V.; Muthuramalingam, R.; Ayyadurai, S.; Abdel-Wahab, A.; Sub Kwak, B.; Kang, M.; Sreekantan, S. Fe_3O_4-Ag_2WO_4: Facile synthesis, characterization and visible light assisted photocatalytic activity. *New J. Chem.* **2017**, *41*, 11722–11730. [CrossRef]
82. Liu, Z.; Chen, F.; Gao, Y.; Liu, Y.; Fang, P.; Wang, S. A novel synthetic route for magnetically retrievable Bi_2WO_6 hierarchical microspheres with enhanced visible photocatalytic performance. *J. Mater. Chem. A* **2013**, *1*, 7027. [CrossRef]
83. Zhou, Y.-X.; Tong, L.; Zeng, X.-H.; Chen, X.-B. Fe_3O_4@Bi_2WO_6 Core–Shell Structured Microspheres: Facile Construction and Magnetically Recyclable Photocatalytic Activity Under Visible-Light. *J. Nanosci. Nanotechnol.* **2015**, *15*, 9868–9873. [CrossRef] [PubMed]
84. Karunakaran, C.; Vinayagamoorthy, P.; Jayabharathi, J. Nonquenching of Charge Carriers by Fe_3O_4 Core in Fe_3O_4/ZnO Nanosheet Photocatalyst. *Langmuir* **2014**, *30*, 15031–15039. [CrossRef]
85. Zhang, J.; Wang, W.-N.; Zhao, M.-L.; Zhang, C.-Y.; Huang, C.-X.; Cheng, S.; Xu, H.-M.; Qian, H.-S. Magnetically Recyclable Fe_3O_4@$Zn_xCd_{1-x}S$ Core–Shell Microspheres for Visible Light-Mediated Photocatalysis. *Langmuir* **2018**, *34*, 9264–9271. [CrossRef] [PubMed]